CFD-Based Study of Steep Irregular Waves for Extreme Wave Spectra

Ankit Aggarwal[1] *, Mayilvahanan Alagan Chella[1] , Hans Bihs[1], Csaba Pákzodi[2], Petter Andreas Berthelsen[2], Øivind A. Arntsen[1]

[1]Department of Civil and Environmental Engineering, Norwegian University of Science and Technology
Trondheim, Norway
[2]SINTEF Ocean
Trondheim, Norway

International Journal of Offshore and Polar Engineering, 2018, **28** 2, pp. 164-170.
DOI: http://dx.doi.org/10.17736/ijope.2018.ak26

Abstract

Offshore structures are exposed to irregular sea states consisting of breaking and nonbreaking waves. They perpetually experience extreme wave loads after installation in the open ocean. Thus, the study of steep waves is an important factor in the design of offshore structures. In the present study, a numerical investigation is performed to study steep irregular waves in deep water. The irregular waves are generated using the Torsethaugen spectrum, which is a double-peaked spectrum defined for a locally fully developed sea and which takes both the sea and swell waves into account. Thus, the generated waves can be very steep. The numerical investigation of such steep waves is quite challenging because of their high wave steepness and wave–wave interaction. The present investigation is performed using the open-source computational fluid dynamics (CFD) model. The wave generation and propagation of steep irregular waves in the numerical model are validated by comparing the numerical wave spectrum with the experimental input wave spectrum. The numerical results are in good agreement with experimental results. The changes in the spectral wave density during the wave propagation are studied. Further, the double-hinged flap wavemaker is also tested and validated by comparing the numerical and experimental free-surface elevations over time. The time and the frequency domain analysis is also performed to investigate the changes in the free-surface horizontal velocity. Complex flow features during the wave propagation are well captured by the CFD model.

Keywords: Irregular waves, CFD, double-peaked spectrum, double-hinged flap wavemaker.

*Corresponding author, ankit.aggarwal@ntnu.no

Postprint, published in International Journal of Offshore and Polar Engineering, doi:http://dx.doi.org/10.17736/ijope.2018.ak26

1 Introduction

Offshore wind turbines are exposed to extreme irregular sea states. Extreme waves exert extreme hydrodynamic loads on substructures. Thus, the study of such irregular waves is very important in the design of offshore wind turbines. Several experimental and field investigations have been performed in the past to study extreme waves. Such spectra exhibit two peaks, because of the presence of swell and wind waves. Ochi and Hubble (1976) carried out a statistical analysis of 800 measured wave spectra in the North Atlantic Ocean. They derived a six-parameter double-peaked spectrum that is composed of two parts: the first primarily includes the low-frequency wave components and the second contains the high-frequency wave components. Each part of the wave spectrum is represented by three parameters. The six-parameter spectrum represents almost all stages of the sea conditions associated with a storm. Guedes Soares and Nolasco (1992) analyzed wave data from the North Atlantic and the North Sea and proposed a four-parameter double-peaked spectrum. This double-peaked spectrum was formulated by superimposing individual spectral components of the JONSWAP-type single-peaked spectrum. Torsethaugen (1996) used a similar approach of combining two individual JONSWAP spectra for different frequency ranges; instead of averaging, Torsethaugen used other parameters of the JONSWAP spectrum. Violante-Carvalho et al. (2004) studied the influence of swell waves on wind waves by using buoy data measurements in deep water in the South Atlantic sea. Other researchers have also made efforts in this direction to study the double-peaked spectra (Masson, 1993); dobson. Pákozdi et al. (2015) performed laboratory experiments with breaking irregular waves using the Toresthuagen spectrum to measure the global impact loads on offshore structures. Their study highlighted the importance of double-peaked spectra for a better representation of extreme sea states. The real state is composed of the sea and swell. Most of the widely used spectra, like the JONSWAP and PM spectra, do not consider both sea states. The Torsethaugen spectrum provides an opportunity to study the real state more closely (Torsethaugen, 1996).

Computational fluid dynamics (CFD) can be used as an effective tool to study such double-peaked spectra. CFD has been used previously by many researchers to numerically study breaking and nonbreaking waves. Alagan Chella et al. (2015, 2016, 2017) and Kamath et al. (2016) studied breaking waves and breaking wave forces on a vertical slender cylinder over an impermeable sloping seabed and they observed a good match with experiments. Bihs et al. (2016*b*) investigated the interaction of breaking waves with tandem cylinders under different impact scenarios. Bredmose and Jacobsen (2010) investigated breaking wave impacts on offshore wind turbine foundations for the focused wave groups using CFD. They compared the numerical and theoretical free surface and wave forces in the time-domain by using the linear reconstruction of waves. Östman et al. (2015) performed CFD investigations with irregular waves using the Torsethaugen spectrum. They compared their numerical results with experimental data (Pákozdi et al., 2015). They found a reasonable match between CFD and experiments. However, the numerical extreme wave crest heights were lower, and wave phases were not correct in comparison with experiments. Also, the wave energy content for the higher frequencies was not accurately captured in comparison with the experiments.

In the present paper, an attempt has been made to numerically model the extreme waves. The experiments were performed for 1:60 scaled $H_s = 20$ m and $T_p = 20.1$ s (Pákozdi et al., 2015). Most previous CFD studies with irregular waves are limited to the single-peaked spectra and nonextreme wave heights. The present paper used two different wave generation methods.

To the best of our knowledge, this is the first study wherein a double-peaked wave spectrum is used as input to generate irregular waves. The goal of the present study is to numerically investigate irregular wave generation and propagation of the steep irregular waves generated using the double-peaked spectrum (i.e., the Torsethaugen spectrum) by using the open-source CFD model REEF3D (Bihs et al., 2016*a*). The wave generation and propagation are tested by comparing the numerical wave spectrum with the experimental wave spectrum in a numerical wave tank (NWT) without any structures. The numerical results are in good agreement with the experimental results. Next, the double-hinged flap wavemaker theory in the numerical model is validated by comparing the numerical wave free-surface elevation in the time-domain with the experimental data (Pákozdi et al., 2015). The reason for modeling the double-hinged wavemaker is to simulate the experimental wave conditions as closely as possible. Usually, the experimental tests are more economically expensive and time-consuming. The numerical double-hinged flapmaker can be used as the preliminary test before running the experiments for all cases. This could be beneficial both time- and money-wise. Further, the changes in the horizontal velocities at the free surface during wave propagation are also investigated in the time- and frequency-domains.

2 Numerical model

The present numerical model is based on the governing equations of fluid dynamics: the continuity equation and the Reynolds averaged Navier–Stokes (RANS) equations with the assumption of an incompressible fluid given as

$$\frac{\partial u_i}{\partial x_i} = 0 \tag{1}$$

$$\frac{\partial u_i}{\partial t} + u_j \frac{\partial u_i}{\partial x_j} = -\frac{1}{\rho}\frac{\partial p}{\partial x_i} + \frac{\partial}{\partial x_j}\left[(\nu + \nu_t)\left(\frac{\partial u_i}{\partial x_j} + \frac{\partial u_j}{\partial x_i}\right)\right] + g_i \tag{2}$$

where u is the velocity averaged over time t; ρ is the fluid density; p is the pressure; ν is the kinematic viscosity; ν_t is the eddy viscosity; i and j denote the indices in the x and y directions, respectively; and g_i is the acceleration due to gravity.

The numerical model uses the fifth-order finite difference weighted essentially nonoscillatory (WENO) scheme in multispace dimensions for spatial discretization (Jiang and Peng, 2000). The third-order total variation diminishing (TVD) Runge–Kutta scheme is used for the time discretization (Shu and Oscher, 1988). An adaptive time-stepping scheme is used in the numerical model (Griebel et al., 1998). The present study uses the $k-\omega$ model (Wilcox, 1994) along with the RANS equation. The level set method is used to capture the free surface (Osher and Sethian, 1988). Detailed information about the numerical model can be obtained in Bihs et al. (2016*a*). In the numerical model, the irregular waves are generated by the super-positioning of the linear regular waves components (Aggarwal et al. (2016*a*,*b*)). The second-order irregular wave theory is used here (Schaffer, 1996).The present study uses the experimental spectrum as an input for the numerical model, which is generated by using the Torsethaugen spectrum (Torsethaugen, 1996). The input values to the spectrum are the significant wave height H_s and the peak period T_p.

The double-hinged flap wavemaker is also tested and validated in the present work. The schematic sketch of the double-hinged flap wavemaker is shown in Fig. 1. The paddle motion is directed positively toward the wall and negatively toward the water. Angles for both hinges with respect to time are given as input to the numerical model (β for H1 and $\beta + \gamma$ for H2). The angles are converted to distance vector $X(z)$ using

$$sign = -\frac{\theta}{|\theta|}; X(z) = sign * |sin\theta| \tag{3}$$

where θ is the angle at the hinge measured from the vertical (β for H1 and $\beta + \gamma$ for H2). The velocity $U(z,t)$, which is the inflow boundary condition, is calculated as

$$U(z,t) = \frac{\delta X(z)}{\delta t} \tag{4}$$

where $X(z)$ varies as a function of depth (normalized with respect to the flap length). The values are zero at the hinge and maximum at the tip of the flap.

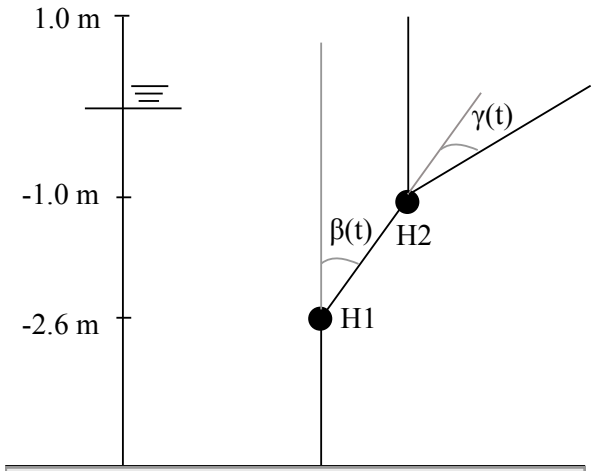

Figure 1: A schematic sketch of the double-hinged flap wavemaker

3 Setup of the NWT

The numerical tests are conducted in a two-dimensional NWT as shown in Fig. 2. The numerical model is validated by comparing the numerical results with the experimental data (Pákozdi et al., 2015). The NWT used in the simulations is 56 m long and 15 m high with a water depth of 10 m. Five wave gauges and three velocity probes are placed along the length of the NWT in order to study the changes in the wave surface elevation and free-surface wave velocity.

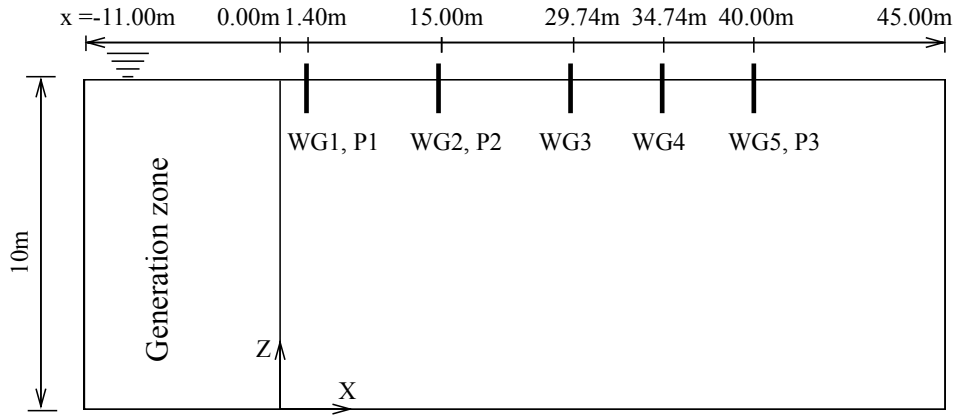

Figure 2: Setup of the NWT (side view)

4 Results

4.1 Grid refinement study with wave spectrum input

The grid refinement study is conducted for the wave spectra in the NWT under steep irregular waves. The numerical tests are performed for the significant wave height $H_s = 0.345$ m and the peak period $T_p = 2.6$ s with four different grid sizes ($dx = 0.10$ m, 0.05 m, 0.01 m, and 0.005 m) for the grid refinement study. Figure 3 presents the comparison of numerical and experimental spectral wave density over the frequency for different grid sizes at WG1, WG2, WG3, and WG4. For the wave gauge located next to the wave generation zone (WG1), the numerical results with $dx = 0.10$ m and 0.05 m are not captured properly in comparison with the experimental results in the high-frequency range; also, the numerical peak spectral wave density is lower than the experimental peak spectral wave density by 57.14% and 25.71% at grid sizes $dx = 0.10$ m and 0.05 m, respectively. The results with $dx = 0.01$ m show a good match with the experimental ranges in most of the frequency range. The difference between the experimental and numerical peak spectral wave densities reduces to 3.92% (Fig. 3a). However, the numerical wave spectrum is relatively narrow compared to the experimental case, and some difference is observed between experimental and numerical spectra in higher frequencies (0.81–1.00 Hz). The results with $dx = 0.005$ m show a slight improvement, and the difference between the experimental and numerical peak spectral wave densities reduces to 2.22%. However, the improvement in results is not very significant at $dx = 0.005$ m. The numerical results converge at $dx = 0.01$ m. Similar behavior is observed for the comparison between the other wave gauges (Figs. 3b–d). For WG3, for $dx = 0.01$ m and 0.005 m, the numerical spectrum is narrower (0.2–0.78 Hz) compared to the experimental spectrum (0.2–1.1 Hz). The spectral peaks and spectral wave densities at all wave gauges are well captured by the numerical model in most of the frequency range when compared with the experimental spectrum. A decrease in the peak value of spectral wave density is noticed in both numerical and experimental spectra during the wave propagation. The secondary peaks are observed at all wave gauge locations in both the experimental and numerical results. The peak spectral wave density for WG4 is lower than that for the wave gauge located next to the generation zone (WG1) because of wave–wave interactions leading to some steep

waves. These steep waves are very close to breaking and, thus, lose some energy during this process, resulting in lower peak spectral wave density at the wave gauge located close to the end of the wave tank (WG4). The nonlinear energy transfer to higher harmonics takes place. Therefore, the primary peak is reduced, and some secondary peaks are observed in the higher frequencies, which means that the contribution of shorter waves becomes significant when higher-order wave–wave interaction occurs. The numerical spectrum cannot capture the waves in the highest frequency range (0.9–1.2 Hz), possibly because the numerical results employ the second-order irregular wave theory. However, even higher-order components in the irregular wave train could result from the steepening of the wave crest and wave–wave interactions.

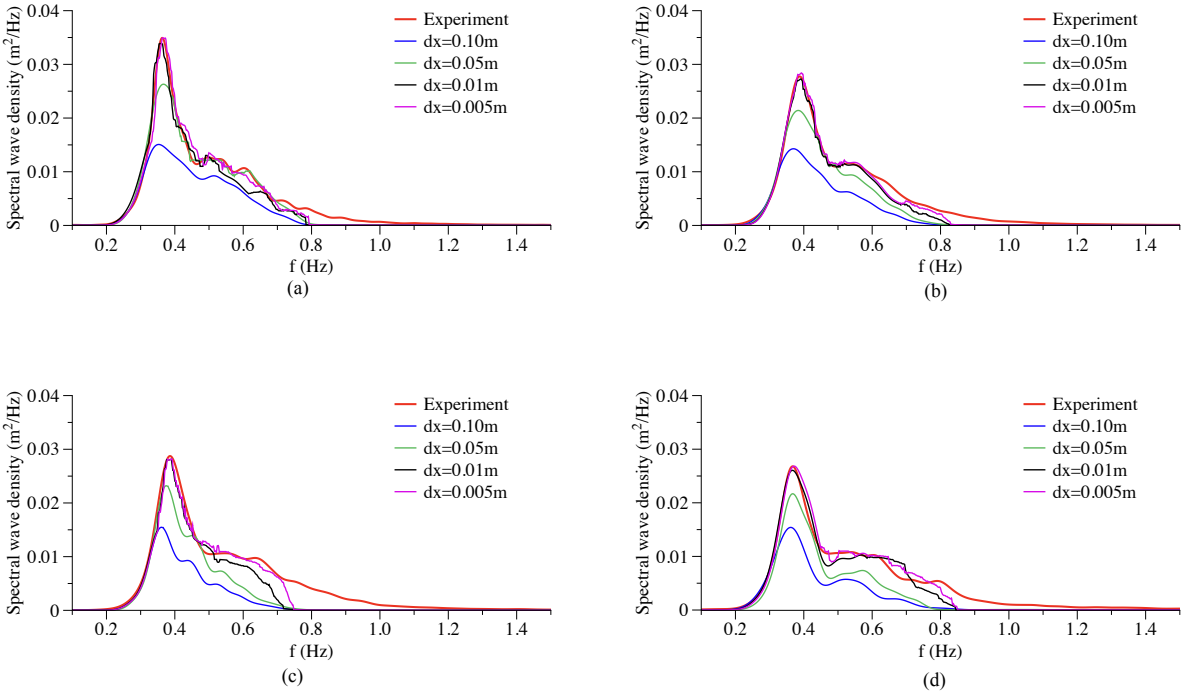

Figure 3: Comparison of the numerical results with different grid sizes and the experimental data (Pákozdi et al., 2015) for the wave spectra at (a) WG1, (b) WG2, (c) WG3, and (d) WG4

4.2 Grid refinement study for double-hinged flap wavemaker

In this part of the paper, the steep irregular wave generation using the double-hinged flap wavemaker theory is tested and validated. The input angle signals for the upper and lower flaps from the experiments are used as inputs for the double-hinged flap wavemaker in the numerical model. The numerical tests are performed for the significant wave height H_s = 0.345 m and T_p = 2.6 s with four different grid sizes (dx = 0.10 m, 0.05 m, 0.01 m, and 0.005 m) for the grid refinement study. In the CFD simulations, the waves are numerically generated using 43 s of wave flap signal. Two extreme wave events are generated here using the signals from the experiments. Figure 4 presents the comparison of numerical and experimental wave free-surface elevation (m) over time (s) for three different grid sizes around the steepest wave

crest for extreme events 1 and 2. For extreme event 1, a difference of 14.82% and 6.5% is observed between the experimental and numerical crests for grid sizes $dx = 0.10$ m and 0.05 m, respectively. The difference between the experimental and numerical crest heights for extreme event 1 reduces to 0.04% and 0.02% for grid sizes $dx = 0.01$ m and 0.005 m, respectively. There is almost no observed phase difference between the experimental and numerical extreme events at fine grids $dx = 0.10$ m and 0.005 m around the steep wave crest (Fig. 4a). Similar behavior is observed for extreme event 2. The difference between the numerical and experimental wave crest heights for the extreme event is 36.4% and 26.56% for the grid sizes $dx = 0.10$ m and 0.05 m, respectively. This difference reduces to 9.81% and 8.97% at grid sizes $dx = 0.01$ m and 0.005 m, respectively. The phase information is also captured reasonably well (Fig. 4b). The improvement in the results is not very significant with $dx = 0.005$ m compared to $dx = 0.01$ m. The numerical results converge at $dx = 0.01$ m.

Figure 5 presents the comparison of experimental and numerical ($dx = 0.01$ m) results for

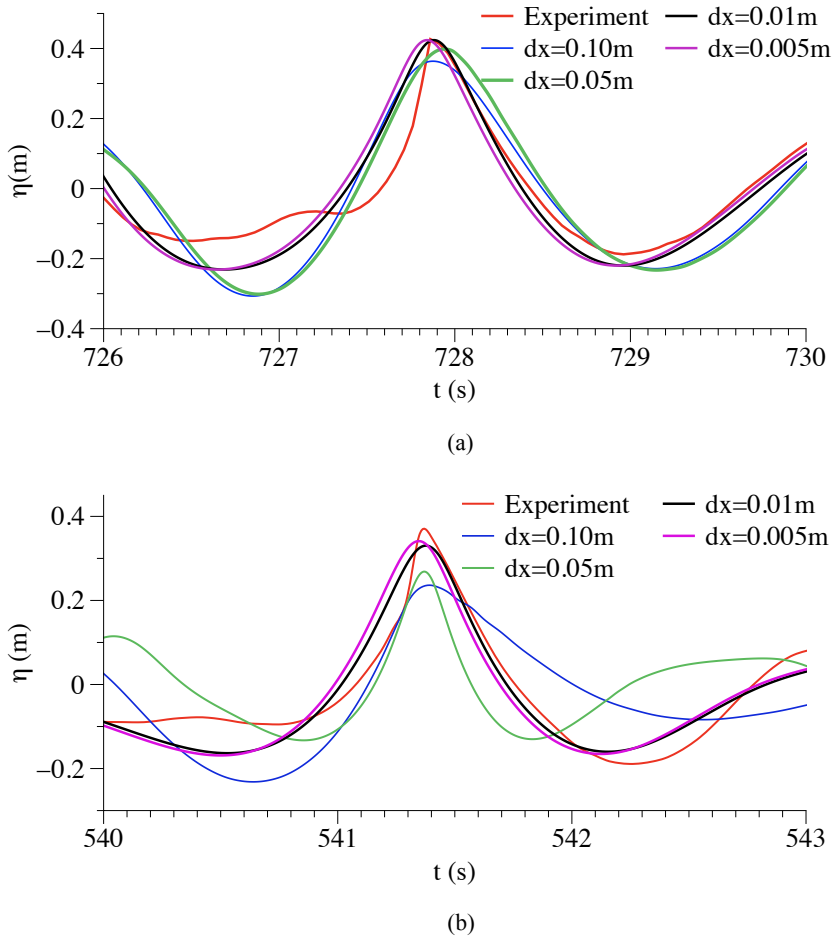

Figure 4: Comparison of numerical and experimental wave free-surface elevation for different grid sizes during (a) extreme event 1 and (b) extreme event 2

the wave free-surface elevation over a longer time-series. For extreme event 1, the numerical

results are in good agreement with the experimental results for most of the time-series. The wave crest peaks for the steep waves are captured in the numerical model with good accuracy when compared with the experimental data (Fig. 5a). For extreme event 2, behavior similar to that for extreme event 1 is observed. The wave propagation and peaks of the wave crests are in good agreement with the experimental data. However, note that the numerical peak for steepest wave in this case is slightly lower than in the experiments. Also, for some parts of the time-series, the wave troughs are slightly overpredicted by the numerical model in comparison with the experiments, and wave phases are in slight disagreement with the experiments. It is possible that the energy transfer between the wave crests is simply sufficient to increase the local wave steepness after the extreme event point when other instabilities, associated with maximum phase velocities, lead to phase differences for the preceding wave crests.

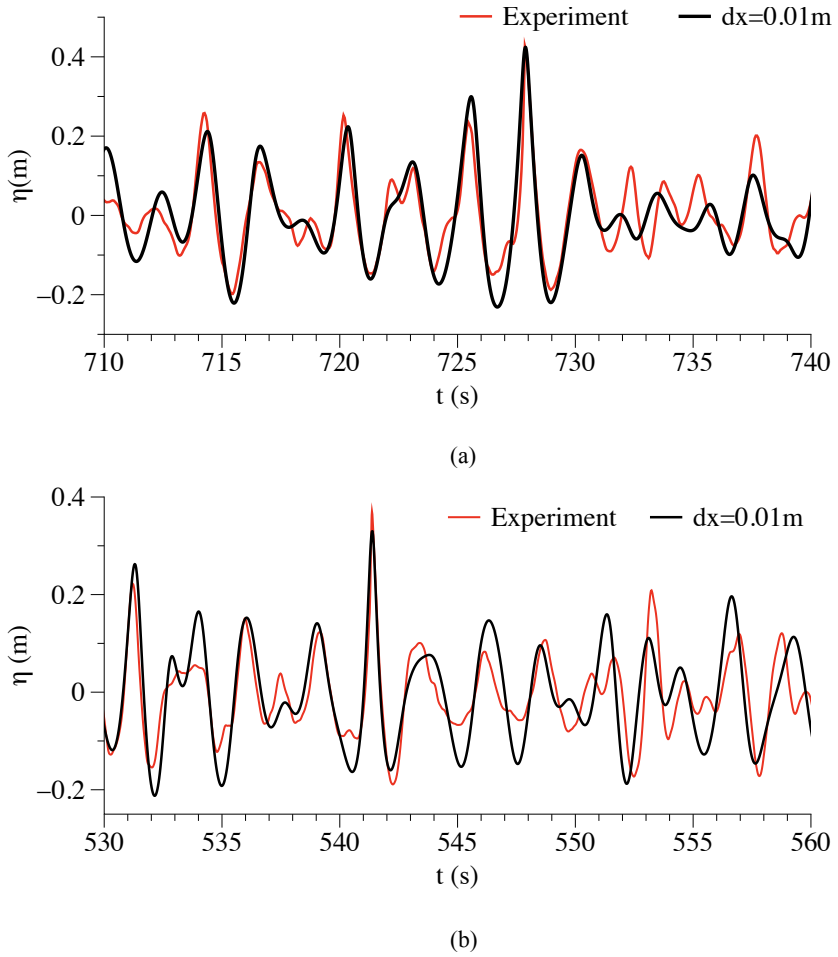

Figure 5: Comparison of numerical and experimental wave free-surface elevation for dx = 0.01 m for longer time series during (a) extreme event 1 and (b) extreme event 2

5 Changes in free-surface horizontal velocity

A transformation of the free-surface wave velocity is observed during the wave propagation. In this section of the paper, the variation of the horizontal component of particle velocity (at the free surface) during the wave propagation in the NWT is investigated. Figure 6 presents the variation of numerical velocity (m/s) over time (s) at different velocity probe locations. Observe that, for extreme event 1, the velocities computed at the probe located at $x = 15$ m (P2) have higher values of peak velocity compared with the velocities measured at the probe located next to the wave generation zone (P1). This might be due to the generation of steeper waves (with larger wave heights and larger velocities) during wave propagation. The peak velocities measured at the velocity probe located at $x = 40$ m (P3) show lower crest values compared with the velocities measured at the probe located at $x = 15$ m (P2) (Fig. 6a). Similar behavior is observed for extreme event 2 (Fig. 6b).

Further, the frequency domain analysis is performed to study the changes in the horizontal

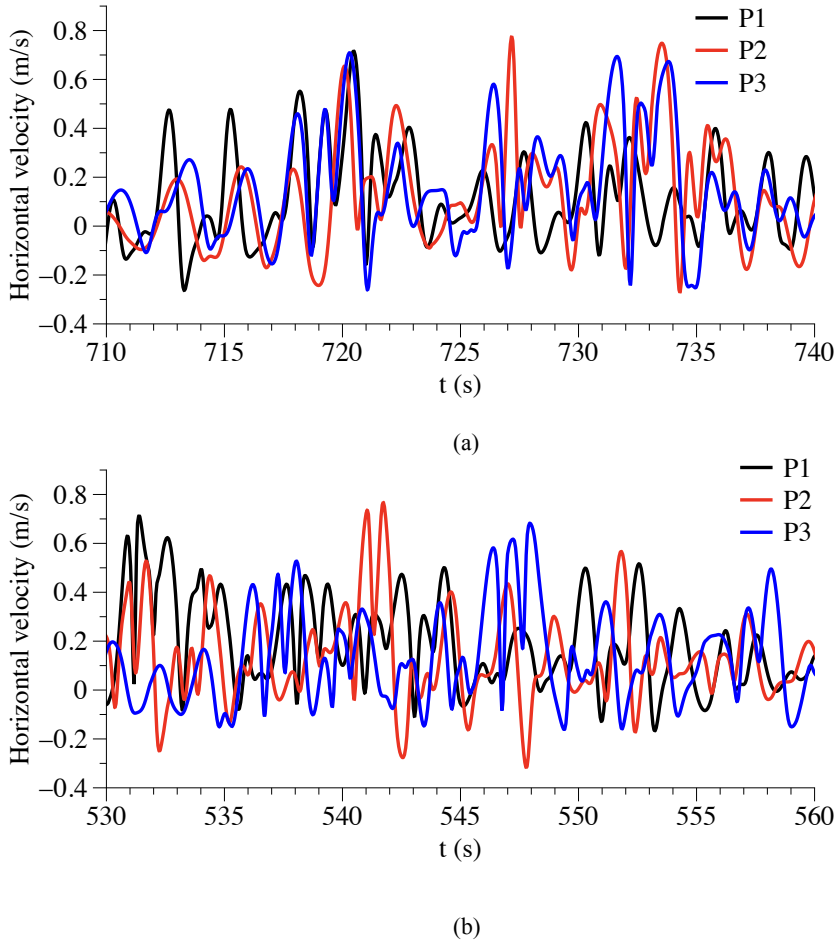

Figure 6: Numerical horizontal velocity with respect to time during (a) extreme event 1 and (b) extreme event 2

component of velocity (at the free surface). Figure 7 presents the velocity spectral density

(m^2/s) over frequency (Hz) at different velocity probes along the NWT. Two spectral peaks are observed in the frequency spectrum. For extreme event 1, the primary peak is observed at $f = 0.42$ Hz with a value of 0.063 m^2/s, while the secondary peak occurs at $f = 0.80$ Hz with a value of 0.0396 m^2/s for the velocity probe located next to the wave generation zone (P1). The value of the primary peak is increased by 8.7%, and the value of secondary peak is decreased by 62%; also, a shift of 0.02 Hz is observed in the location of secondary peak occurrence for the probe located at $x = 15$ m (P2). A decrease in the values of both primary and secondary peaks is observed for the velocity probe located at $x = 40$ m (P3). Also, more than one secondary peak is noticed (Fig. 7a). Similar behavior is observed for extreme event 2: an increase of 54.23% is noted in the primary spectral peak for the probe located at $x = 15$ m (P2) compared with the primary spectral peak at the velocity probe located next to the wave generation zone (P1). This increase for extreme event 2 is higher compared with extreme event 1, but the spectral peak values in general for extreme event 1 are larger than for extreme event 2. This might be due to a higher steepest wave crest during extreme event 1 (Fig. 5). This again corresponds to the energy transfer and energy loss due to wave breaking and wave–wave interaction to higher frequencies range, which leads to the decrease in the spectral velocity peaks. The primary spectral velocity peak at P2 is much higher than that at P1 or P3 for extreme event 2 compared with extreme event 1. However, the spectral peak value for extreme event 2 at P2 is lower than that for extreme event 1. The reason might be that a higher number of wave–wave interactions have taken place for extreme event 2 than for extreme event 1. As extreme event 1 has already occurred, it is possible that some of the waves that led to extreme event 1 with relatively larger wave heights and velocities are present in the irregular wave train, which might have possibly contributed toward the higher primary spectral peak for extreme event 2.

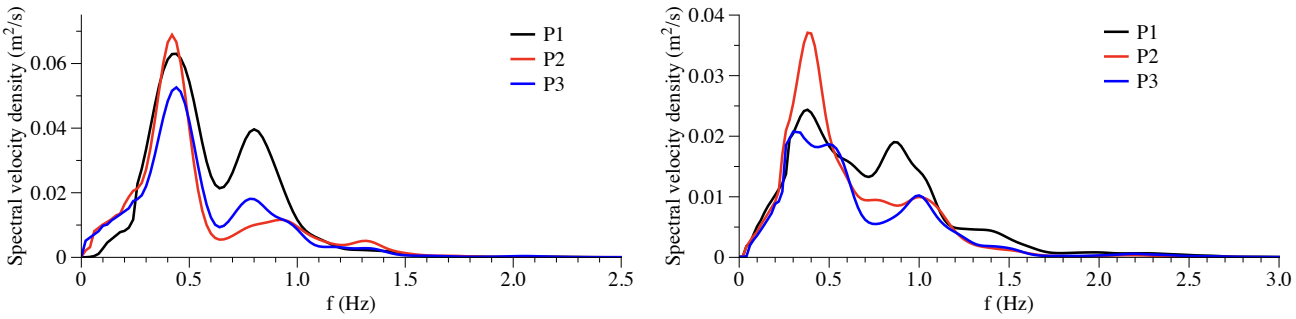

Figure 7: Numerical velocity spectral density over frequency during (a) extreme event 1 and (b) extreme event 2

6 Free-surface changes

Figure 8 presents the simulated free-surface changes with velocity magnitude (m/s) variation during the propagation of irregular steep waves in the NWT at different time-steps. Figure 8a shows a two-dimensional view of the irregular wave propagation along the whole domain

of the NWT at $t = 38.27$ s. The waves with different velocities in the irregular free surface are observed. Figure 8b shows a zoomed view around the steep wave: note that the velocity of the wave crest starts to get larger compared to the other waves. In the next time step, at $t = 38.49$ s, the steep wave (extreme event 1) with very high velocity and elevation is observed (Fig. 8c). After the wave crest reaches its maximum height and attains maximum crest velocity, as shown in Fig. 8c, the velocities and the wave heights start to decrease again (Figs. 8d and 8e). A uniform inflow, similar to conditions for a bore propagating onto a weak current, leads to an internal-flow pattern, with turbulence spreading downward into the incident flow. An inflow that has the fully developed profile of a steady turbulent flow gives rise to separation under the front of the wave and a substantially different flow field, although without any significant change in the surface profile.

7 Conclusions

The CFD-based numerical model is used to model irregular steep waves for the extreme wave spectrum. The numerical model is validated with measured data for simulating steep irregular waves using the double-peaked Torsethaugen spectrum. A grid refinement study is performed in order to study the effect of the grid size on the numerical results for the wave spectral density. A good match is observed between the experimental and numerical results. The wave spectrum shows two peaks for all wave gauges. The value of the primary peak is slightly lower for the wave gauge located close to the end of wave tank as compared to the wave gauge located next to the wave generation zone, due to the loss of energy during wave propagation. Further, the numerical double-hinged flap wavemaker is validated by comparing the wave free-surface elevation time series with the experimental data. This is performed for two extreme events as measured in the experiments. A grid refinement study is also conducted to study the effect of grid sizes on the wave free-surface elevation. Note that numerical values for the steepest wave crest are in good agreement with the experimental peak crest values. In the next section, investigations are performed to study the changes in the horizontal velocity at the free surface. The following conclusions can be drawn from the study:

- For the steep irregular waves propagating in deep water, as the waves propagate, they undergo wave–wave interaction that increases nonlinearity in the wave spectrum. The energy from the primary peak is transferred toward higher frequencies and the contribution of secondary peaks and shorter waves increases.

- The numerical model represents well the wave crest peaks and wave phases until the extreme events. After the extreme events, the extreme wave crest with large wave height interacts with preceding wave crests and further increases wave nonlinearity. This might be the reason that wave phases are not represented well after the extreme wave event occurs.

- The horizontal wave velocities and the spectral velocity densities are affected by the wave spectral density. The wave heights for extreme waves increase, which leads to an increase in the primary spectral peak for the second wave probe. Some of the waves close to the beach either break or are close to breaking, which leads to dissipation of wave energy and thus to reduction in the spectral velocity density peaks.

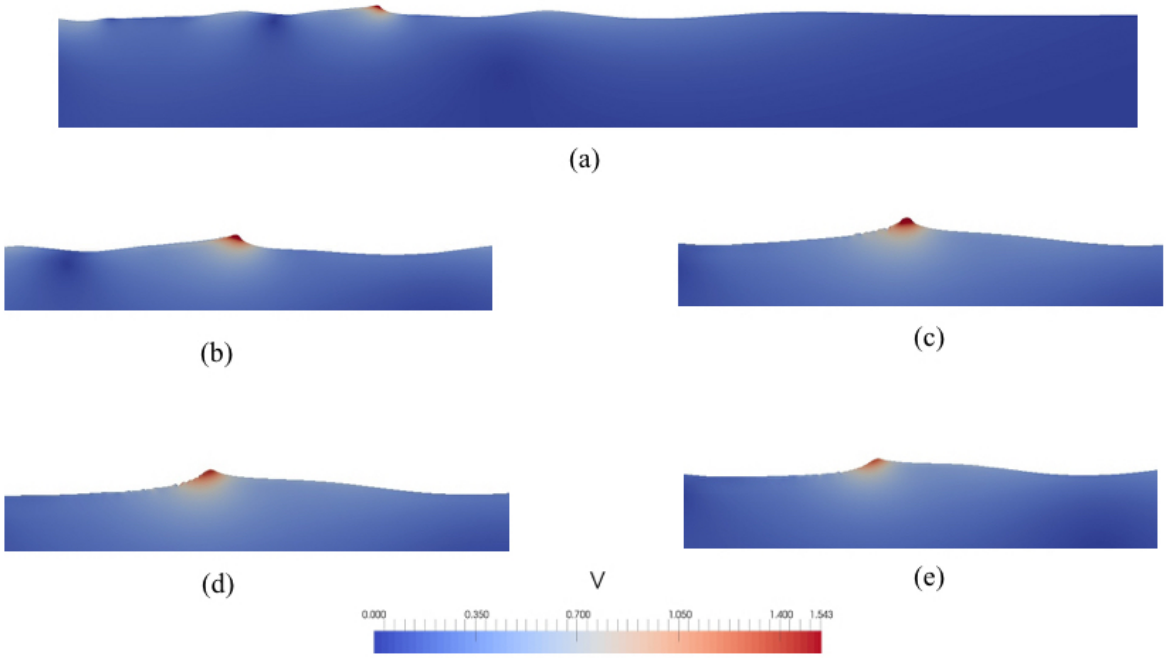

Figure 8: Simulated free-surface changes with velocity magnitude (m/s) variation during the propagation of the irregular steep wave along the wave tank at (a) $t = 38.27$ s and with zoomed-in-view at (b) $t = 38.27$ s, (c) $t = 38.49$ s, (d) $t = 38.69$ s, and (e) $t = 38.81$ s

- The effect of turbulence increases with increasing wave nonlinearity due to nonlinear energy transfer and dissipation. This is an important factor and taking it into account for the design of offshore and coastal structures is recommended.

Acknowledgements

The research work has been funded by the Research Council of Norway through the project "Hydrodynamic Loads on Offshore Wind Turbine Substructures" (project number 246810). The authors gratefully acknowledge the computing time granted by NOTUR (project number NN2620k).

References

Aggarwal, A., Alagan Chella, M., Kamath, A., Bihs, H. and Arntsen. A., O. (2016*a*). Irregular wave forces on a large vertical circular cylinder. *Energy Procedia*, **94**, 504–516.

Aggarwal, A., Alagan Chella, M., Kamath, A., Bihs, H. and Arntsen. A., O. (2016*b*). Numerical simulation of irregular wave forces on a horizontal cylinder. *ASME 2016 35th International Conference on Ocean, Offshore and Arctic Engineering, Volume 2: CFD and VIV.*

Alagan Chella, M., Bihs, H. and Myrhaug, D. (2015). Characteristics and profile asymmetry properties of waves breaking over an impermeable submerged reef. *Coastal engineering*, **100**, 26–36.

Alagan Chella, M., Bihs, H., Myrhaug, D. and Michael, M. (2016). Hydrodynamic characteristics and geometric properties of plunging and spilling breakers over impermeable slopes. *Ocean Modelling*, **103**, 53–72.

Alagan Chella, M., Bihs, H., Myrhaug, D. and Michael, M. (2017). Breaking solitary waves and breaking wave forces on a vertically mounted slender cylinder over an impermeable sloping seabed. *Journal of Ocean Engineering and Marine Energy*, **3**, 1–19.

Bihs, H., Kamath, A., Alagan Chella, M., Aggarwal, A. and Arntsen. A., O. (2016*a*). A new level set numerical wave tank with improved density interpolation for complex wave hydrodynamics. *Computers and fluids*, **140**, 191–208.

Bihs, H., Kamath, A., Alagan Chella, M. and Arntsen. A., O. (2016*b*). Breaking-wave interaction with tandem cylinders under different impact scenarios. *Journal of Waterway, Port, Coastal, and Ocean Engineering*, **142**, 1–14.

Bredmose, H. and Jacobsen, G.N. (2010). Breaking wave impacts on offshore wind turbine foundations: focused wave groups using CFD. *Proceedings of OMAE, June 6-11.*

Griebel, M., Dornseifer, T. and Neunhoeffer, T. (1998). *Numerical Simulations in Fluid Dynamics*. SIAM.

Guedes Soares, C. and Nolasco, M. (1992). Spectral modeling of sea states with multiple wave systems. *Journal of Offshore Mechanics and Arctic Engineering*, **114**, 278–284.

Jiang, G.S. and Peng, D. (2000). Weighted ENO schemes for Hamilton Jacobi equations. *SIAM Journal of Scientific Computing*, **21**, 2126–2143.

Kamath, A., Chella, A., M., H., B. and Arntsen, A., Ø. (2016). Breaking wave interaction with a vertical cylinder and the effect of breaker location. *Ocean Engineering*, **128**, 105–115.

Masson, D. (1993). On the nonlinear coupling between swell and wind waves. *Journal of Physical Oceanography*, **23**, 1249–58.

Ochi, M. and Hubble, E. (1976). On six-parameter wave spectra. *In Proceedings of 15th Coastal Engineering Conference ASCE*, **321**.

Osher, S. and Sethian, J.A. (1988). Fronts propagating with curvature- dependent speed: Algorithms based on hamilton-jacobi formulations. *Journal of Computational Physics*, **79**, 12–49.

Östman, A., Pákozdi, C., Stansberg, T., C., Fagertun, T., J. and Vestbøstad, M.T. (2015). CFD simulation and validation of breaking wave impact events in irregular sea states. *Proceedings of International Society of Offshore and Polar Engineering.*

Pákozdi, C., Visscher, J., H., Stansberg, C. and Fagertun, J. (2015). Experimental investigation of global wave impact loads in steep random seas. *Proceedings of International Society of Offshore and Polar Engineering.*

Schaffer, H.A. (1996). Second-order wavemaker theory for irregular waves. *Ocean Engineering*, **23(1)**, 47–88.

Shu, C.W. and Oscher, S. (1988). Efficient implementation of essentially non-oscillatory shock capturing schemes ii. *Journal of Computational Physics*, **77**, 439–71.

Torsethaugen, K. (1996). Model for double peaked wave spectrum. *SINTEF report STF22 A96204*.

Violante-Carvalho, N., Ocampo-Torres, F. and Robinson, I. (2004). Buoy observations of the influence of swell on wind waves in the open ocean. *Journal of Computational Physics*, **26**, 49–60.

Wilcox, D. (1994). Turbulence modeling for CFD. . *DCW Industries Inc. La Canada, California.*